Mild-Temperature Responsive Nanocatalyst for Controlled Drug Release-Enhanced Photothermal and Catalytic Therapy

Mengmeng Xu [a], Yuan Liu [a], Xiaoqi Xie [a], Paul, D. Topham [b], Yuandong Zeng [a], Jilai Zhan [a], LinGe Wang [a,*] and Qianqian Yu [a,*]

[a] South China Advanced Institute for Soft Matter Science and Technology, School of Emergent Soft Matter, Guangdong Provincial Key Laboratory of Functional and Intelligent Hybrid Materials and Devices, South China University of Technology, Guangzhou 510640, P. R. China.

[b] Chemical Engineering and Applied Chemistry, School of Infrastructure and Sustainable Engineering, College of Engineering and Physical Sciences, Aston University, Birmingham, B4 7ET, UK.

ABSTRACT:

Owing to the advantages of the *in situ* production of toxic agents through catalytic reactions, nanocatalytic therapy has arisen as a highly potential strategy for cancer therapeutics in recent years. However, the insufficient amount of endogenous hydrogen peroxide (H_2O_2) in the tumor microenvironment commonly limits their catalytic efficacy. Here, we employed carbon vesicle nanoparticles (CV NPs) with high near-infrared (NIR, 808 nm) photothermal conversion efficiency as carriers. Ultrafine platinum iron alloy nanoparticles (PtFe NPs) were grown *in situ* on the CV NPs, where the highly porous nature of the resultant CV@PtFe NPs was employed to encapsulate a drug, β-lapachone (La), and phase-change material (PCM). As a novel multifunctional nanocatalyst CV@PtFe/(La-PCM) NPs can exhibit a NIR-triggered photothermal effect and activate cellular heat shock response, which upregulates the downstream NQO1 via HSP70/NQO1 axis to facilitate bio-reduction of the concurrently melted and released La. by oxygen (O_2) participation to enhanced intracellular H_2O_2 level, promote the bimetallic PtFe-based nanocatalyst, catalyze H_2O_2 into highly toxic hydroxyl radicals (•OH) for catalytic therapy. Our results show that this multifunctional nanocatalyst can be used as a versatile synergistic therapeutic agent with NIR-enhanced nanocatalytic tumor therapy by tumor-specific H_2O_2 amplification and mild-temperature photothermal therapy, which holds promising potential for targeted cancer treatment.

Keywords: Nanocatalyst, Mild photothermal, β-lapachone, Phase change material, Tumor therapy.

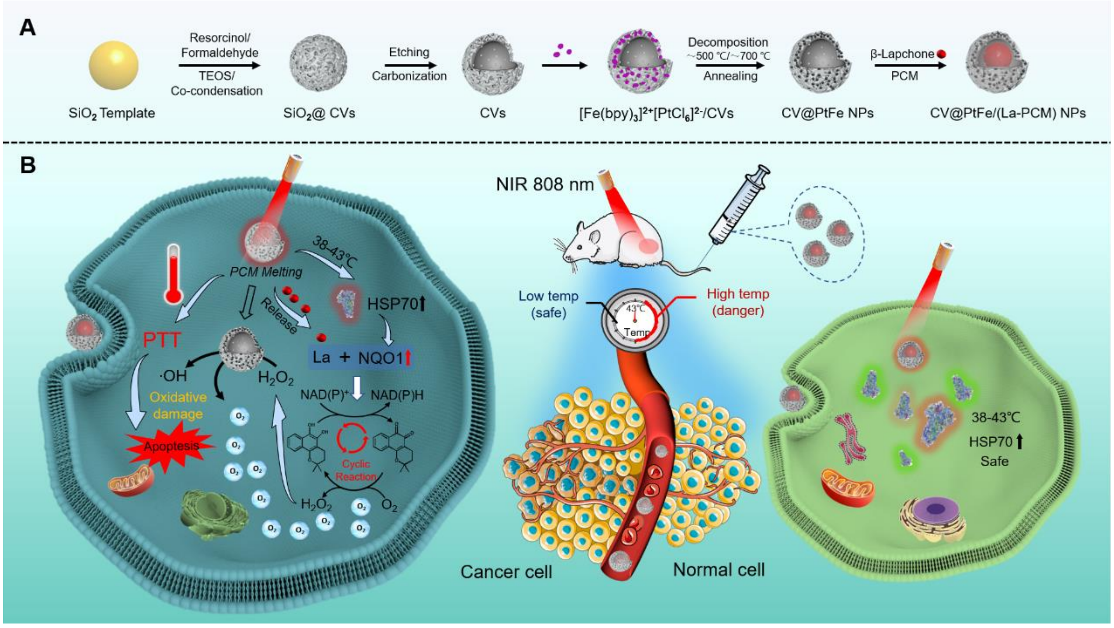

Scheme 1. (A) Preparation route of the nanocatalyst [CV@PtFe/(La-PCM) NPs] and

(B) the schematic illustration of its combination therapy of tumor.

1. Introduction

Cancer, one of the most serious diseases, poses a major threat to human health with its high morbidity and mortality rates [1-4]. Traditional cancer treatment usually includes chemotherapy, surgery and radiation therapy [5, 6]. However, each of these approaches has its drawbacks, such as unsatisfactory tumor elimination, poor target specificity, and its inevitable lethal side effects [7]. Thus, it is urgent to explore novel agents for effective cancer treatments. After extensive research alternative treatments have emerged in recently years, including photodynamic therapy (PDT) [8, 9], ultrasonic therapy, photothermal therapy (PTT) [10-13], and nanocatalytic therapy [14-16]. Among the various nano-therapy systems, nanocatalytic therapy has received increasing attention. Nanocatalysts are used to facilitate catalytic reactions in the tumor microenvironment (TME), where convert H_2O_2 is converted to hydroxyl radicals (•OH) by a typical Fenton or Fenton-like reaction, achieving high effectiveness, noninvasiveness, and high spatiotemporal selectivity [17-19]. Recently, platinum iron alloy nanoparticles (PtFe NPs) have attracted increased popularity in this field due to their unique intrinsic catalytic properties and suitability for application in biosensors [20, 21], and cancer therapy [22-24]. However, the effectiveness of these strategies is not sustainable due to limited intratumoral H_2O_2 in the TME [25, 26]. To address these limitations, abundant efforts have been devoted to intratumoral H_2O_2 supply for relatively enhanced efficiency of tumor therapy [16, 27]. Although both the direct delivery of H_2O_2 and the employment of peroxide materials can increase the H_2O_2

concentration in tumors to some extent, they do not supply H_2O_2 continuously [28]. Therefore, a better approach could be to stimulate *in situ* H_2O_2 generation to induce the concomitant specific response. In addition, a coalition of multiple therapeutic modalities with synergistic properties can achieve a better curative effect than a single modality [29-32].

One of the most common strategies for improving the efficiency of nanocatalytic therapy is to increase the local temperature at the tumor site [33, 34]. PTT uses photothermal agents to convert near infrared region (NIR) light energy into heat to increase the local temperature and destroy tumor cells [35-39]. Despite the rapid development of the PTT strategy to enhance the efficiency of the nanocatalytic therapy in recent years. However, photothermal reagent-mediated reactions can cause damage to normal tissues when the local temperature is too high (>45 °C) and could activate a heat shock response in tumor cells, enhancing the expression of heat shock proteins (HSPs) [40-42]. HSP70, one of the most important contributors to photothermal resistance in the HSP family, could stabilize and upregulate nicotinamide adenine dinucleotide (phosphate) (NAD(P)H): quinone oxidoreductase protein (NQO1) in tumor cells [28, 43-45]. Tumor cells overexpress NAD(P)H: NQO1 enzyme, which can convert β-lapachone (La, an FDA-approved antitumor drug) to hydroquinone [46]. The intracellular La cyclic reaction is completed by oxygen participation to oxidize hydroquinone back to La with H_2O_2 generation [47]. Thus, using La to amplify the H_2O_2 level in tumor cells, one could greatly increase the nanocatalytic therapy efficacy. Considering the central role of NQO1 in regulating tumor redox homeostasis, photothermal agent-mediated PTT at relatively low temperature (<45 °C) may help to increase the intracellular ROS levels [40, 48, 49]. Although multimodal therapies based on a combination of PTT and nanocatalytic therapy have great potential in the management of tumors, coordinating individual treatment activities and further scaling up treatment effects constitute a significant challenge and scientific barrier for realization of this approach. Meanwhile, a new type of functional material, phase change material (PCM), has been found to be able to quickly respond to temperature and transform into a transparent liquid phase for a controllable release of drugs [50-53].

Herein, we report a multifunctional carbon vesicle-based nanocatalyst, using CV@PtFe/(La-PCM) NPs for sustained stimulation of endogenous H_2O_2 production, rationally designed for synergistic nanocatalytic and mild-temperature PPT therapy. Ultrasmall PtFe alloys were grown *in situ* on the carbon vesicle nanoparticles (CV NPs). In parallel, β-lapachone (La) was held within a biocompatible organic phase change material (PCM, a mixture of lauric and stearic acids with a eutectic point of 39 °C) before loading into the porous of CV@PtFe NPs. Attributed to the enhanced permeability and retention (EPR) effect, tumor accumulation was significantly improved, as the ultrasmall PtFe NPs can effectively catalyze the generation of •OH and O_2 from endogenous H_2O_2. The CV NPs with good photothermal efficiency can generate heat under the irradiation of NIR at 808 nm, which can not only directly inhibit tumor growth, but also enhance the expression of NQO1 through the HSP70/NQO1 axis. The simultaneous elevated temperature melts the PCM and speeds up the release of La, which can be formed through NQO1-mediated bio-reduction and leads to redox cycling of H_2O_2. The continuously compensate for the production of H_2O_2 and amplify the catalytic effect of ultrasmall PtFe NPs to further convert into highly toxic •OH, ultimately led to local and effective tumor eradication. Thus, this study provides a new multimodal treatment strategy for catalytic cancer therapy with remarkable tumor specificity and enhanced therapy.

2. Methods and materials

2.1. Materials

2,2′-Bipyridine (bpy, ≥99%), 2,2′,6′,2″-terpyridine (terpy, ≥98%), iron (II) sulfate heptahydrate ($FeSO_4 \cdot 7H_2O$, ≥99.0%), 1,10-phenanthroline (phen, ≥99%), Tris (4,7-diphenylL-1,10-phenanthroline) ruthenium (II) dichloride ($[Ru(dpp)_3]Cl_2$), RDPP), 3,3′,5,5′-tetramethylbenzidine (TMB), chloroplatinic acid hexahydrate ($H_2PtCl_6 \cdot 6H_2O$, ≥37.50% Pt basis), lauric acids, stearic acids, H_2O_2 solution (30%), ammonia (aqueous solution, 28 wt%), sodium hydroxide (NaOH, ≥96%), resorcinol, 5,5-dimethyl-1-pyrroline *N*-oxide (DMPO), dimethyl sulfoxide (DMSO), TEOS and formaldehyde (aqueous solution, 37 wt%), ethanol (anhydrous, 99.9%) and isopropanol (>99.99%) were purchased from Sigma-Aldrich. Calcein-AM /PI apoptosis detection kit, 1% penicillin/streptomycin, 1% phenylmethanesulfonyl fluoride, Cell Counting Kit-8 (CCK-8), 2′,7′-dichlorofluorescein diacetate (DCFH-DA), 4,6-diamidino-2-phenylindole (DAPI), BCA protein assay kit, enhanced chemiluminescence kit, 1′,3,3′-tetraethyl-imidacarbocyanine (JC-1) kit were bought from Beyotime Biotechnology (Shanghai, China). Dulbecco minimum essential medium (DMEM), streptomycin, penicillin and fetal bovine serum (FBS) were all purchased from Gibco (Invitrogen, USA). Ultrapure deionized water (Milli-Q, resistivity of 18.2 MΩ) was used throughout.

2.2. Characterization

The morphology of the nanomaterials was characterized by transmission electron microscopy (TEM, JEM-1400, 200 kV), scanning electron microscopy (SEM, JEOL, Japan) equipped with EDS (energy dispersive spectrometer), and X-ray diffraction (XRD) patterns were recorded on the diffractometer (PANalytical B.V. Holland). An ultraviolet visible (UV-vis) absorption spectrophotometer (UV-3600, Shimadzu Corporation, Japan) and fluorescence spectrophotometer (RF-5301 PC, Shimadzu, Japan) were used for the characterization of La release and O_2 generation. The photothermal effect was measured using an 808 nm laser (HW808AD2000-100F, China). Temperature changes were recorded using an infrared thermal camera (Fortic225, IRS Systems Inc.). Zeta potential and dynamic light scattering (DLS) were characterized by NanoBrook Omni. The surface area and microporous analyzer were measured via N_2 adsorption−desorption isotherms (beishide, 3H-2000PM1). Electron spin resonance (ESR) was carried out on a Bruker E500-10/12 spectrometer (Germany) at room temperature to capture the •OH generated in the reaction.

2.3. Fabrication of carbon vesicle nanoparticles (CV NPs)

CV NPs were fabricated via a one-pot method [54]. In a typical process, TEOS (1 mL) was added into a solution of ammonia (1.0 mL), ethanol (50 mL), and water (10 mL). The mixture was stirred for 24 h at room temperature to prepare SiO_2 nanoparticles. Resorcinol (90 mg) and formaldehyde (0.20 mL) were then added, and allowed to stand for 5 h before a certain amount of TEOS was introduced. After another 24 h, the reaction system containing the as-fabricated SiO_2@RF-SiO_2 nanoparticles was transferred into a Teflon-lined autoclave and was heated for 12 h at 100 °C. The solid product was collected through centrifugation, and was annealed at 800 °C for 1 h under nitrogen flow. CV NPs were formed after removal of the silica template via NaOH solution etching. The resultant CV NPs were washed with water/ethanol mixture via centrifugation, and were re-dispersed in isopropanol for further use.

2.4. Synthesis of $[Fe(bpy)_3][PtCl_6]$ compound (PtFe compound)

PtFe compound was fabricated as follows [55]. Briefly, $FeSO_4 \cdot 7H_2O$ (9.3 mg·mL^{-1}, 15 mL) deionized water solution, and 1.5 mmol of 2,2′-bipyridine (15.62 mg·mL^{-1}, 15 mL) ethanol (99.9%) solution were mixed to form dark-red $[Fe(bpy)_3]SO_4$, which was stirred overnight at room temperature. Into the dark-red solution, $H_2PtCl_6 \cdot 6H_2O$ (8.63 mg·mL^{-1}, 30 mL) ethanolic solution was added instantly. Brighter-red PtFe compound was precipitated immediately after addition of the Pt solution without any difference after 5 h of stirring at room temperature. The red precipitate can be easily separated by short-time centrifugation (10 000 rpm, 10 min). Even with several washing steps on the PtFe compound with ethanol, the solid precipitate can be completely obtained after centrifugation. The precipitate was then dried in an oven at 40 °C overnight. A fine powder can be obtained by grinding the dried precipitate in a mortar with a pestle.

2.5. Synthesis of CV@PtFe NPs and CV@PtFe/(La-PCM) NPs.

The freshly prepared PtFe compound (0.45 g·mL^{-1}, 80 mL) deionized water solutions [55]. The resulting mixture was sonicated for 10 min and stirred for 2 h, after which, the aqueous CV NPs solution (4 mg·mL^{-1}, 10 mL) was added dropwise. PtFe compound was well-attached on the CV NPs after mixing for 2 h followed by freeze drying. The composite containing PtFe compound grains on CV NPs foam was then thermally treated at 700 °C for 6 h in an argon flow of 100 sccm, during which, complete wetting and decomposition of the PtFe compound occurred on the surface of the CV NPs, forming atomically ordered PtFe alloy nanoparticles on CV, denoted as CV@PtFe NPs. The next step was to load the PCM and β-lapachone (La) into the CV@PtFe NPs. In a typical process, 2.5 mg of stearic acid, 10 mg of lauric acid, and 5 mg of La were dissolved in 0.5 mL of DMSO under magnetic stirring for 30 min. After the addition of 2 mg of CV@PtFe NPs, the suspension was kept in a vacuum oven for 10 min to remove any unwanted air trapped in the nanocapsules. The suspension was then centrifuged at 10,000 rpm for 5 min, and the supernatant was discarded, followed by two rounds of washing with DMSO to remove any excess La and fatty acids. Then, 1 mL of water was introduced into the above precipitate to solidify the fatty acids and retain the La inside the nanocapsules. It should be emphasized that washing with DMSO is essential to reduce surface adsorption.

2.6. In vitro *photothermal effect of CV@PtFe/(La-PCM) NPs*

To estimate the photothermal performance of CV@PtFe/(La-PCM) NPs, the aqueous solutions of CV@PtFe/(La-PCM) NPs at different concentrations were irradiated under near infrared (808 nm, 1.0 $W\cdot cm^{-2}$), and an infrared thermal camera was used to record the temperature with time. The temperature change of CV@PtFe/(La-PCM) NPs under laser irradiation over five light on/off cycles was also monitored to assess the photothermal stability. Then the photothermal conversion efficiency (η) was calculated according to the previously reported papers [56, 57].

2.7. In Vitro *cellular uptake*

The cellular uptake was assessed by the confocal laser scanning microscopy (CLSM). Typically, cells were seeded in confocal dishes at a density of 3×10^4 cells/well and cultured overnight. Then, cells were incubated with Cy7-labeled CV@PtFe/(La-PCM) NPs for 1, 2 and 4 h. After incubation, the culture medium was removed and the cells were washed with PBS three times. Cell nuclei were stained with DAPI for 5 min and washed with PBS again. then the resulting cells were analyzed by CLSM.

2.8. Cytotoxicity and cell apoptosis evaluation

2.8.1 CCK-8 assay

We used a typical CCK-8 kit assay to measure the *in vitro* cytotoxicity of CV@PtFe/(La-PCM) NPs in Human Umbilical Vein Endothelial Cell (HUVEC), NIH/3T3 Cells and 4T1 cells. Cells were placed into a 96-well microplate filled with

10 % fetal bovine serum and 1 % penicillin, and kept at 37 °C with 5 % CO_2. Then, the CV@PtFe/(La-PCM) NPs with different concentrations were added into each well for 24 h of incubation before the cell viability was assayed via the CCK-8 method.

2.8.2 Live/dead cells staining assay

4T1 cells were seeded into confocal dishes (10^6 cells/well) and cultured for 24 h (37 °C, 5% CO_2). Then, CV NPs, CV@PtFe NPs, and CV@PtFe/(La-PCM) NPs in DMEM media were added to respective wells. After another 24 h of incubation, cells were stained with Calcein-AM (live cells) and propidium iodide (PI, dead/late apoptotic cells), according to the manufacturer's suggested protocol. Finally, cellular fluorescence was monitored on CLSM.

2.8.3 Analysis of the change of mitochondrial membrane potential

To investigate the mitochondrial membrane potential, 4T1 cells were seeded in confocal dishes at a density of 1×10^5 cells and incubated for 12 h. Subsequently, the DMEM was replaced with freshly acidified DMEM containing H_2O_2 (100 μM), CV NPs, CV@PtFe NPs or CV@PtFe/(La-PCM) NPs, followed by 4 h incubation. Furthermore, one of each of these samples was exposed to 808 nm NIR laser irradiation (1.0 $W\cdot cm^{-2}$) for 5 min, and compared to its corresponding counterpart which had not been exposed. After another 20 h, the culture medium was replaced with a JC-1 staining solution according to the manufacturer's protocol. The cells were then washed twice with PBS and treated according to the JC-1 kit. Finally, the fluorescence of the cells was analyzed using a CLSM.

2.9. Western blot analysis

To analyze the expression levels of key proteins in photothermal-controlled therapy, 4T1 cells were seeded on a 6-well plate (3×10^5/well) overnight, and the incubation media was afterwards replaced for different treatments with laser or without laser (fresh media as control). Then, 4T1 cells were lysed with RIPA lysis buffer containing 1% phenylmethanesulfonyl fluoride (protease inhibitor cocktail), The lysates were centrifuged at 12,000 rpm (15 min, 4 °C) and the BCA protein assay kit was used to analyzed total protein content. After protein denaturation at 100 °C for 10 min, different samples were loaded onto SDS-PAGE, before the proteins were transferred to poly(vinylidene fluoride) (PVDF) membranes, and then blocked with 5 % skim milk for 12 h at 4 °C. Subsequently, the samples were blocked with primary antibodies overnight at 4 °C and secondary antibodies for 2 h. After washing with TBST three times, the PVDF membranes were visualized by an enhanced chemiluminescence kit according to the manufacturer's instructions.

2.10. Catalytic performance evaluation

2.10.1 In vitro *and intracellular O_2 generation*

The catalase-like activity of CV@PtFe/(La-PCM) NPs was detected by measured O_2 generation with a portable dissolved oxygen meter. CV@PtFe/(La-PCM) NPs were dispersed in water containing 100×10^{-6} M H_2O_2 and the oxygen levels were recorded over time. The dissolved O_2 in H_2O_2 solution was previously removed by N_2 purging for 20 min. O_2 generation through catalyzing a high level of intracellular H_2O_2 in tumor cells was investigated by confocal fluorescence imaging with an O_2 sensing probe, $[(Ru(dpp)_3)]Cl_2$ (RDPP). The fluorescence of this agent is strongly quenched by O_2. 4T1 cells were cultured at a density of 5×10^6 cells per well in confocal microscopy dishes for 24 h. Then, the cells were incubated with RDPP (5×10^{-6} M) for 4 h and with CV@PtFe/(La-PCM) NPs for another 4 h. The fluorescent signals of RDPP (Ex 488 nm, Em 610 nm) in cells were then observed and imaged under CLSM.

2.10.2 Detection of in vitro •OH production

First, CV NPs, CV@PtFe NPs and CV@PtFe/(La-PCM) NPs were dispersed in 1 mL solutions with H_2O_2 under NIR or without. 10 mM TMB solution was added. After that, the absorbances of TMB were measured at 652 nm using a UV−vis spectrophotometer. Electron spin resonance (ESR) spectroscopy provides direct evidence for the presence of •OH, which can be captured by DMPO, a widely used radical trapping agent. CV NPs, CV@PtFe NPs and CV@PtFe/(La-PCM) NPs of solutions with or without NIR laser irradiation, and DMPO (25 mM) was added. ESR spectra were recorded from the beginning of the reaction.

2.10.3 Intracellular ROS level detection

The ROS-sensitive probe, 2,7-dichlorofluorescein diacetate (DCFH-DA), was used to detect intracellular ROS generation levels in 4T1 cells. Briefly, 4T1 cells were seeded in confocal microscopy dishes at a density of 2×10^5 cells per well and cultured for 24 h. The cells were further incubated with CV@PtFe/(La-PCM) NPs or with 808 nm laser irradiation for 5 min and continued for 24 h after being replaced with a fresh medium containing DCFH-DA for 30 min. Finally, the fluorescence of the cells was analyzed by CLSM.

2.11. In vivo *therapeutic evaluation of CV@PtFe/(La-PCM) NPs*

Healthy female BALB/c nude mice (four weeks old, ≈20 g) were purchased from the Institutional Animal Care and Use Committee of SCUT (AEC No. 2020048). The guidelines of the Regional Ethics Committee for Animal Experiments were strictly followed to handle all of the mice. Initially, the 4T1 tumor-bearing nude mouse model was established by subcutaneously injecting 100 μL of 4T1 cell suspension ($\sim 10^6$ cells) and the tumor volume reached about 100 mm^2 after 7 days of growth. Subsequently, these mice were randomly divided into four groups (n=4): Control, CV NPs, CV@PtFe NPs and CV@PtFe/(La-PCM) NPs group were injected with 100 μL (2.5 $mg \cdot kg^{-1}$) via the tail vein on days 1, 3, 5 and irradiated by the 808 nm laser (1.0 $W \cdot cm^{-2}$) or not (non-irradiated). The tumor volume and bodyweight of the mice were recorded daily to explore the treatment efficiency and toxicity in each group. The tumor volume was calculated based of a standard protocol (volume = $L \times W^2 \times 0.5$), in which L and W are the length and width of the tumor, respectively. After 15 days of tumor therapy, the mice were euthanized and the tumors in each group were removed and weighed. At the same time, the main organs and the tumors were collected for histological analysis. Finally, the tumor tissues of mice from each group were collected for further TUNEL, H&E and Ki-67 antibody staining.

2.12. In vivo *fluorescence imaging*

Cy7-labeled CV@PtFe/(La-PCM) NPs were used for *in vivo* imaging. For the synthesis of Cy7-labeled CV@PtFe/(La-PCM) NPs, Cy7 (1 mg·mL^{-1}) were mixed by stirring at room temperature in the dark (24 h). Then, Cy7-CV@PtFe/(La-PCM) NPs were collected through centrifugation and washed with deionized water for further use. Tumor-bearing mice used for *in vivo* imaging had a tumor volume of up to 200 mm^3. For the evaluation of biodistribution of Cy7-CV@PtFe/(La-PCM) NPs, free Cy7 solution was intravenously injected into the mice. Then, the mice fluorescence signal was monitored at designed time points (pre, 2, 4, 8, 12, 24, and 48 h). The tumor and major organs collected from the sacrificed mice were imaged on an IVIS imaging system.

2.13. Statistical analysis

In all tests, the statistical significance (*$p < 0.05$, **$p < 0.01$ and ***$p < 0.001$) between two groups was confirmed via unpaired two-tailed Student's *t*-test embedded in GraphPad Prism 8.0 (GraphPad Software, USA). All data are shown as mean ± standard deviation (SD, n = 3).

3. Results and discussion

3.1. Structures and morphologies of CV@PtFe/(La-PCM) NPs

The synthesis of CV@PtFe/(La-PCM) NPs is shown in Scheme 1A. CV NPs were first prepared by a template method, which involves the growth of resorcinol formaldehyde resin (RF resin) on the SiO_2 template surface, subsequent carbonization and template removal. Monodisperse CV NPs with a uniform diameter of approximately 120 nm were characterized by SEM (Fig. 1A), which is consistent with the DLS results shown in Fig. S1. The TEM images shown in Fig. 1B and Fig. S2 show that CV NPs can be deposited by spray coating, easily applied to complex surfaces and over large areas. Furthermore, the XRD pattern of CV NPs displayed a broad peak around 23.3° and a small peak at 43°, corresponding to the (002) and (100) planes, indicating the graphite-like layered structure (Fig. S3). CV@PtFe NPs were further fabricated using CV NPs as platforms by directly synthesizing PtFe NPs on CV NPs. Firstly, we prepared bimetallic compounds $[Fe(bpy)_3][PtCl_6]$ (bpy = 2,2′-bipyridine) composed of a $[Fe(bpy)_3]^{2+}$ cation and $[PtCl_6]^{2-}$ anion, which can be thermally decomposed into homogeneously alloyed PtFe NPs. The TEM images (Fig. 1C and Fig. S4) confirmed that the morphology of the hybrid nanomaterials was maintained after alloyed PtFe NPs modification. Moreover, The XRD pattern suggests that the PtFe NPs are highly crystalline with a completely different crystal structure from the original $[Fe(bpy)_3][PtCl_6]$ (Fig. 1I and Fig. S5). The SEM image and EDS elemental mapping images of CV@PtFe NPs in Fig.1F and Fig. S6 show the homogeneous and even elemental distribution of Pt and Fe, indicating the successful preparation of CV@PtFe NPs. Moreover, the zeta potential increased from -24.52 mV (CVs NPs) to 10.4 mV (Fig. 1G), indicating that the formation of alloyed PtFe NPs on the CV NPs. Notably, after loading the PtFe NPs, the particle size showed no significant changes. The porous properties were measured via N_2 adsorption−desorption isotherms, as shown in Fig. 1H and Fig. S7. These data show that CV NPs possess a high specific surface area and an average pore size that suggests that the CV NPs could be suitable for loading anticancer drugs. The BET surface area decreased with alloyed PtFe NP modification (CV@PtFe NPs), which demonstrated that the mesoporous channels were partially blocked by PtFe nanoparticles. Crucially, the CV@PtFe NPs pore diameter size was approximately 5.3 nm, which should be ideal for drug loading. The reason was that the La-PCM (β-lapachone mixed with PCM) encapsulation resulted in the average pore size decreasing obviously, which verifies the drug has been successfully encapsulated. Moreover, as shown in Fig. S8, the differential scanning calorimetry (DSC) thermogram showed that PCM exhibited a melting point around 39°C, slightly above the normal human body temperature. In addition, as shown in the UV−vis absorption spectra in Fig. 1E, the characteristic peak at 253 nm confirmed the co-existence of the specific absorption corresponding to CV@PtFe NPs and La. The zeta potential decreased from 10.4 mV (CV@PtFe NPs) to -20.92 mV, which also demonstrated the successful modification with La-PCM (Fig. 1G). As evidenced by TEM and DLS measurements (Fig. 1D and S1), the La-PCM encapsulation did not change the size and morphology of the hybrid nanoparticles. Meanwhile, the CV@PtFe/(La-PCM) NPs show excellent suspension stability in a variety of solvents such as water, PBS, saline, DMEM and FBS (Fig. S9). These results confirm that CV@PtFe/(La-PCM) NPs have been successfully fabricated and have the potential to deliver drugs for nanocatalytic cancer therapy.

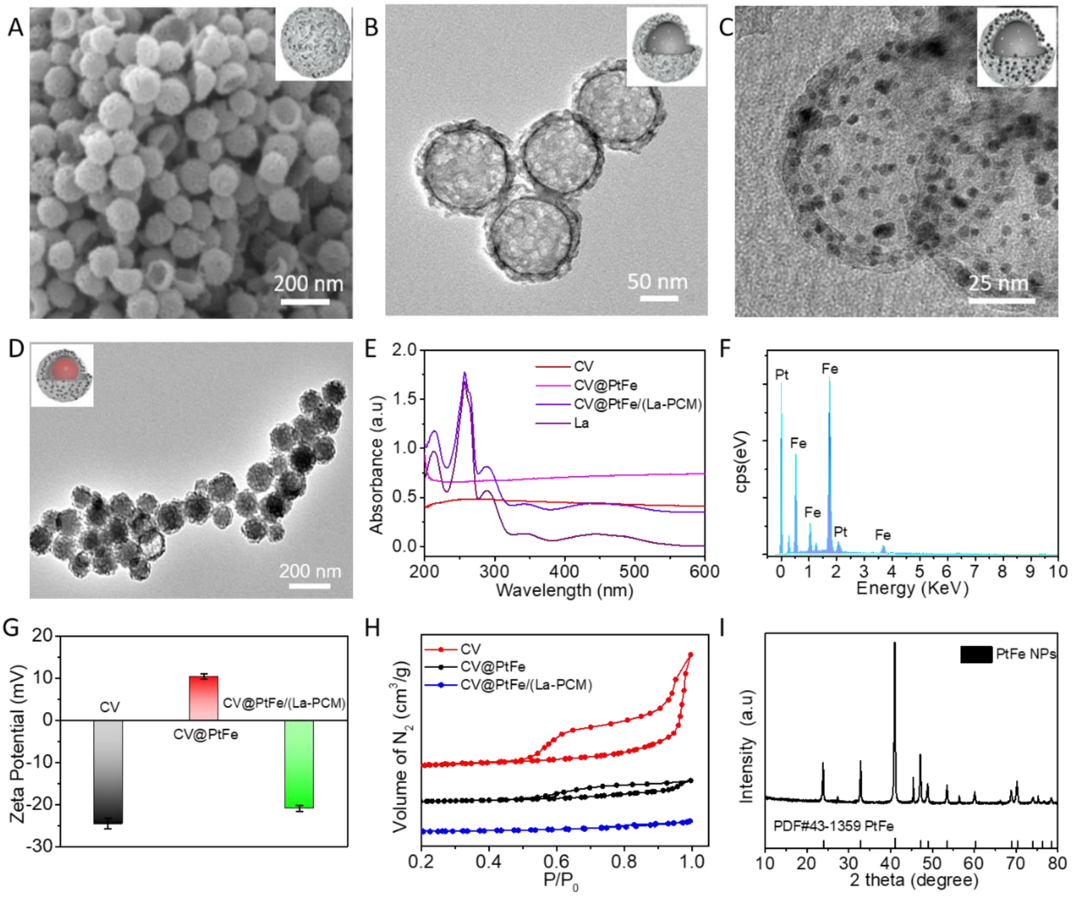

Fig. 1. (A and B) TEM and SEM images of typical CV NPs. (C) TEM image of CV@PtFe NPs. (D) TEM image of CV@PtFe/(La-PCM) NPs. (E) UV–vis absorption spectra of CV NPs, CV@PtFe NPs, CV@PtFe@/(La-PCM) NPs and La. (F) Energy-dispersive X-ray spectroscopy (EDS) of CV@PtFe NPs. (G) Corresponding zeta potential values of the CV NPs, CV@PtFe NPs and CV@PtFe/(La-PCM) NPs. (H) N_2 adsorption−desorption isotherms of CV NPs, CV@PtFe NPs and CV@PtFe/(La-PCM) NPs. (I) Powder XRD pattern of CV@PtFe NPs.

3.2. Photothermal performance of CV@PtFe/(La-PCM) NPs under NIR laser irradiation

Photothermal performance is an important factor in determining the final efficacy of the system. Based on the optical absorbance of CV@PtFe/(La-PCM) NPs in the NIR window (Fig. S10), the photothermal conversion performance of CV@PtFe/(La-PCM) NPs was investigated. The infrared thermal images presented in Fig. 2A visually display the temperature changes under the 808 nm (1.0 $W \cdot cm^{-2}$) laser irradiation at elevated concentrations (0, 25, 50, 100, 150 and 200 $\mu g \cdot mL^{-1}$) and gradually turned yellowish as a function of time, demonstrating the good photothermal conversion efficiency. As shown in Fig. 2B, the temperature profile of the CV@PtFe/(La-PCM) NP solution was estimated by an infrared thermal camera, exhibiting notable optical absorbance at 808 nm and the intensity linearly increased with sample concentration (25~200 $\mu g \cdot mL^{-1}$), while for pure water under the same conditions, the temperature remained almost constant (only a 2.1°C temperature rise). As shown in Fig. 2C, the photothermal performance of CV@PtFe/(La-PCM) NPs showed no obvious change during five heating and cooling cycles (laser off/on), demonstrating that CV@PtFe/(La-PCM) NPs possess good photothermal stability under NIR laser irradiation. To calculate the photothermal conversion efficiency (η), a solution of CV@PtFe/(La-PCM) NPs (100 $\mu g \cdot mL^{-1}$) was irradiated by 808 nm laser (1.0 W cm^{-2}). The η of CV@PtFe/(La-PCM) NPs was calculated as 27.89 %, based on the obtained data (Fig. 2D). Next, we examined the NIR-triggered La release from CV@PtFe/(La-PCM) NPs under 808 nm laser irradiation. Fig. 2E and S11 show that under NIR laser irradiation, the temperature was raised above the eutectic point of the PCM matrix, and La could be released from the melt PCM matrix in its fluid state. Meanwhile, only a small amount of La release was found in the control group without NIR laser irradiation, thus confirming that the

La release is only triggered by NIR induced photothermal effect of CV@PtFe/(La-PCM) NPs.

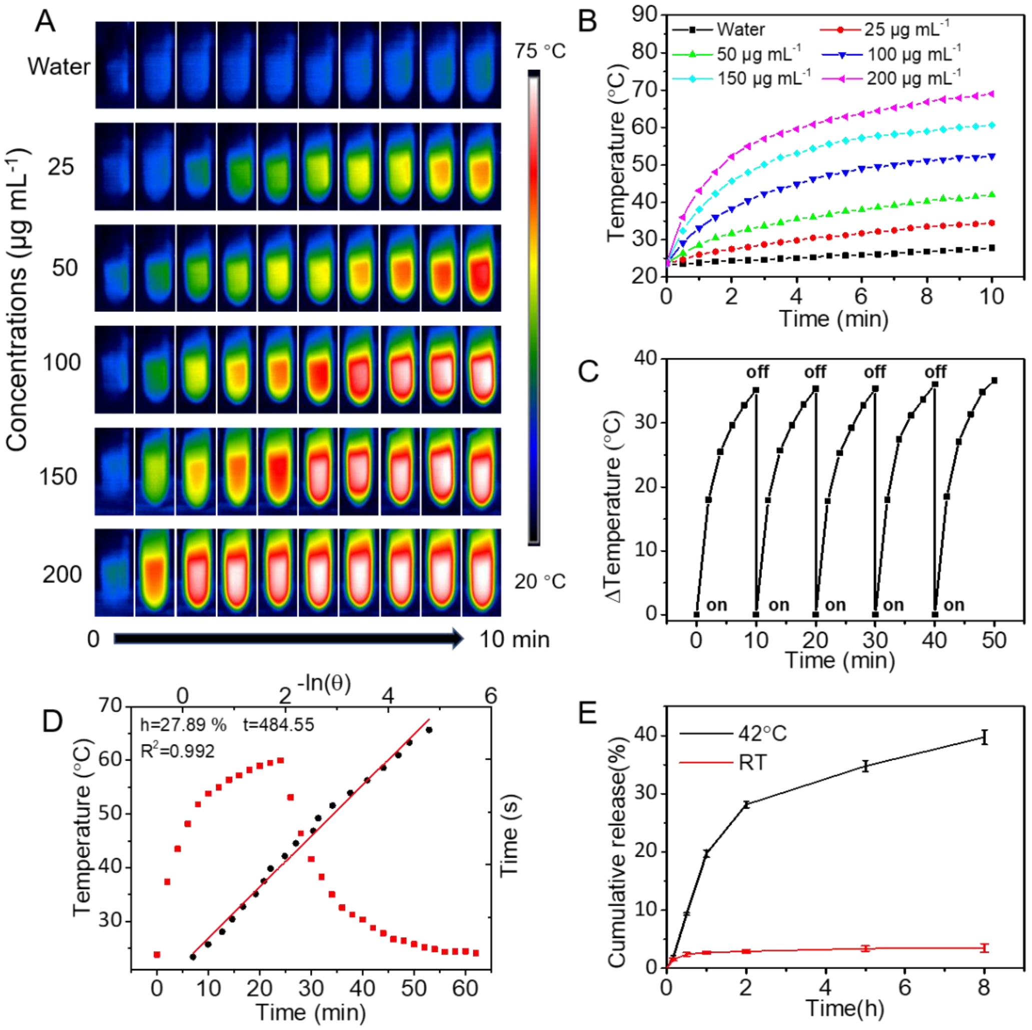

Fig. 2. (A) Corresponding infrared thermal images of panel. (B) Temperature profiles of solutions at different concentrations over a period of 10 minutes under NIR laser irradiation (808 nm, 1.0 W·cm^{-2}). (C) Photothermal stability of CV@PtFe/(La-PCM) NPs exposed to NIR laser irradiation (808 nm, 1.0 W·cm^{-2}) for 5 cycles. (D) Heating and cooling profile of CV@PtFe/(La-PCM) NP aqueous solution and the linear time data obtained from the cooling period. (E) Cumulative La release from the nanocapsules at room temperature (RT) and 42 °C.

3.3 Catalytic activity of CV@PtFe/(La-PCM) NPs

Carbon-based materials are regarded as suitable catalyst support systems since they enable highly dispersed catalytic active sites to be loaded to achieve excellent catalytic performance. For CV@PtFe/(La-PCM) NP-based cascade catalytic activity, the assembled alloyed PtFe NPs on CV@PtFe/(La-PCM) NPs were expected to catalyze •OH in the presence of H_2O_2 (Fig. 3A). We evaluated the catalytic activity of CV@PtFe/(La-PCM) NPs using 3,3′,5,5′-tetramethylbenzidine (TMB) as the substrate since it can be oxidized by •OH to a blue TMB (oxTMB) with an absorbance at 652 nm. As shown in Fig. 3B and Fig. 3C, both CV@PtFe/(La-PCM) NPs contain alloyed PtFe NPs and could catalyze the oxidation of TMB in H_2O_2 solution with a strong absorbance peak at 652 nm, providing evidence of the generation of •OH. In comparison, no oxTMB was observed for the groups with CV NPs only. Additionally, the catalytic performance of the CV@PtFe/(La-PCM) NPs was further investigated by ESR (electron spin resonance) using 5,5-dimethyl1-pyrroline-*N*-oxide (DMPO) as an •OH trapping agent. As illustrated in Fig. 3D, similar results to TMB oxidation were observed, and the typical peak intensity of 1:2:2:1 can be observed after CV@PtFe/(La-PCM) NPs treatment. It should be noted that a dramatically intensified •OH signal was observed in the CV@PtFe/(La-PCM) NPs group with NIR laser irradiation, indicating the photothermal enhanced catalytic performance of CV@PtFe/(La-PCM) NPs to generate abundant quantities of •OH.

Considering the O_2 production has an important effect on the La enhances intracellular H_2O_2 formation under NIR laser irradiation processes. To evaluate the catalase-like activity of CV@PtFe/(La-PCM) NPs, $[Ru(dpp)_3]Cl_2$ (RDPP) was used as a probe to detect O_2 production, as it can undergo fluorescence quenched in the presence of O_2. Fig. 3E demonstrates that the CV@PtFe/(La-PCM) NPs can effectively reduce the fluorescence intensity of RDPP in the presence or absence of NIR laser irradiation compared with the other systems, proving that the CV@PtFe/(La-PCM) NPs can effectively catalyze the production of O_2 from H_2O_2. To further validate the capability of CV@PtFe/(La-PCM) NPs for catalyzed H_2O_2 decomposition into O_2, the dissolved O_2 level in the reaction system was dynamically recorded by using a portable oxygen meter during a 5 minute observation period (Fig. 3F). Compared with the control, the dissolved O_2 concentration in the H_2O_2 solution containing CV@PtFe NPs or CV@PtFe/(La-PCM) NPs increased over time, indicating an effective time-dependent O_2 generation in the presence or absence of NIR laser irradiation. Such local oxygenation mediated by CV@PtFe/(La-PCM) NPs could potentially relieve tumor hypoxia to increase treatment efficacy. Moreover, oxygen bubbles produced by CV@PtFe/(La-PCM) NPs (either free or La encapsulated in the PCM) were visible by eye upon mixing with H_2O_2 (Fig. 3B). In contrast, H_2O_2 alone and pure water were stable with no obvious O_2 release.

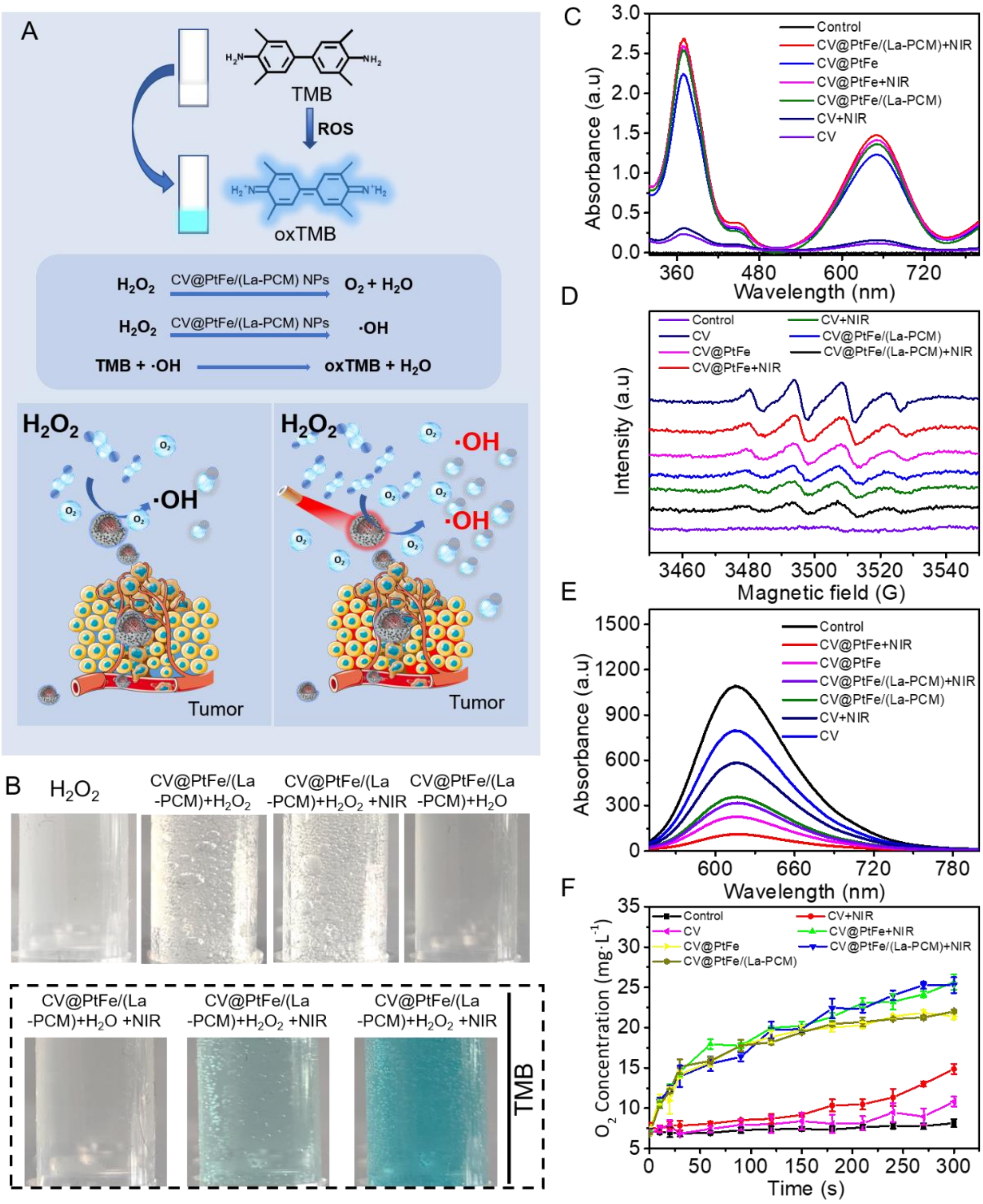

Fig. 3. (A) Schematic depiction of the catalytic activity of CV@PtFe/(La-PCM) NPs and their photothermal catalytic enhancement of •OH and O_2 production. (B) H_2O_2 (10 mM) was decomposed by CV@PtFe/(La-PCM) NPs and the generated O_2 bubbles were seen adsorbed on the inside of the tube wall. (C) UV−vis absorption spectra of CV NPs, CV@PtFe NPs and CV@PtFe/(La-PCM) NPs exposed to NIR laser irradiation or without. (D) ESR spectra of DMPO/•OH adducts collected from H_2O_2 with CV NPs,

CV@PtFe NPs and CV@PtFe/(La-PCM) NPs exposed to NIR laser irradiation or without. (E) Fluorescence spectra of $(Ru(dpp)_3)Cl_2$ after treating with different samples. (F) Generation of O_2 after treating with CV NPs, CV@PtFe NPs and CV@PtFe/(La-PCM) NPs exposed to NIR laser irradiation or without.

3.4 Cellular uptake and cytotoxicity of CV@PtFe/(La-PCM) NPs in vitro

Effective cellular uptake is a prerequisite for the therapeutic function and high efficacy of nanomedicine. Firstly, a fluorescent dye-Cy7 was incorporated into the nanoparticles to enable the cellular uptake behavior of Cy7-labeled CV@PtFe/(La-PCM) NPs in 4T1 breast cancer cells to be probed by CLSM. As shown in Fig. 4A, the cell nuclei were stained with DAPI as blue fluorescence, the green fluorescence in the cytoplasm from Cy7-labeled CV@PtFe/(La-PCM) NPs increased gradually. The results confirmed a greater amount of Cy7-labeled CV@PtFe/(La-PCM) NPs was internalized with incubation time up to 4 h. Prior to the antitumor studies, the *in vivo* safety of the CV@PtFe/(La-PCM) NPs should be carefully evaluated. The CCK-8 assay was applied to quantify the cytotoxicity of the nanocatalyst at different concentrations (0, 6.25, 12.5, 25, 50, and 100 $\mu g \cdot mL^{-1}$) against HUVEC and 3T3 cells. As shown in Fig. 4B and Fig. S12, when treated with CV@PtFe/(La-PCM) NPs at concentrations below 100 $\mu g \cdot mL^{-1}$ for 24 h, the HUVEC and 3T3 cell viability in the nanocatalyst without NIR irradiation group was more than 90%. The results confirmed that the nanocatalyst have good visual biocompatibility under these conditions. Quantitative results of the hemolysis assay are shown in Fig. 4C. Under the physiological environment (pH 7.4), no hemolysis was detected even at the highest concentration of CV@PtFe/(La-PCM) NPs (200 μg·mL^{-1}), suggesting that the nanocatalyst particles were stealth-like during blood transportation and biocompatible to normal tissue, in good agreement with the CCK-8 assay results. The intracellular structure was also visualized using cell fluorescence labeling (Fig. 4D). HUVEC cells treated with CV@PtFe/(La-PCM) NPs at different concentrations had visible nuclei (blue, DAPI) and a developed cytoskeletal structure (green, phalloidin) under confocal laser scanning microscopy (CLSM), suggested their strong cytocompatibility.

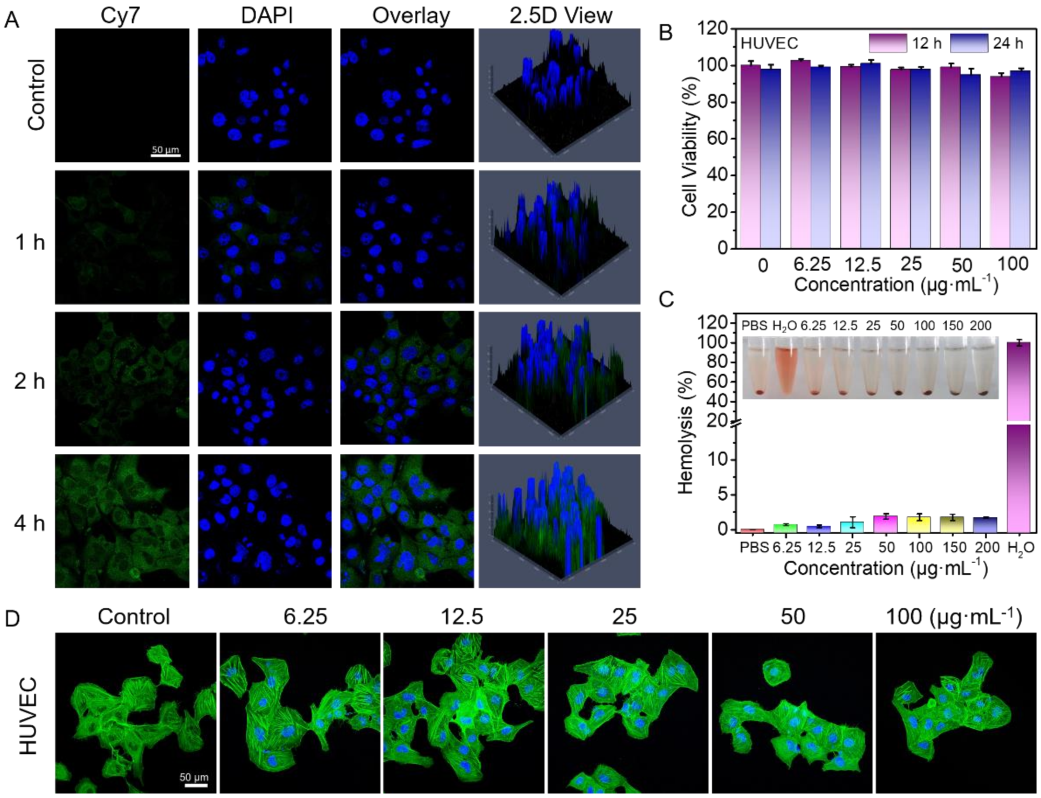

Fig. **4**. (A) CLSM images of 4T1 cells incubated with Cy7-labeled CV@PtFe/(La-PCM) NPs at different time intervals. (B) Relative viabilities of HUVEC cells after being incubated with CV@PtFe/(La-PCM) NPs at varying concentrations for 24 h. (C) Photographic images and quantitative results for membrane-breaking activity of

CV@PtFe/(La-PCM) NPs to mouse RBCs at different concentrations. (D) Morphologies of cells cultured with CV@PtFe/(La-PCM) NPs at different concentrations captured by CLSM (green: Phalloidin; blue: DAPI).

For further biological applications, we then explored the *in vitro* ROS generation by selecting 2′,7′-dichlorodihydrofluorescein diacetate (DCFH-DA) as a fluorescent indicator (Fig. 5A and Fig. 5C). Taking advantage of tumor cell over-expressed (NAD(P)H):(NQO1) enzyme, La generates a cyclic reaction with its reduced form hydroquinone and conversion of O_2 to H_2O_2, which improved •OH generation. Corresponding CLSM images of 4T1 cells treated with CV@PtFe/(La-PCM) NPs under 808 nm NIR laser irradiation, exhibited the strongest fluorescence signal, demonstrating the highest ROS production, compared with the control group and CV@PtFe NPs with NIR laser irradiation. The differences in the intracellular green fluorescence of CV@PtFe NPs with or without NIR laser irradiation, further proved that the photothermal effect can enhance the production of •OH through the use of CV@PtFe NPs. These studies confirmed that ROS amplification is dependent on La and that the photothermal effect of CV@PtFe NPs further assisted catalytic activity, enhancing •OH generation.

Subsequently, the O_2-generation capability of CV@PtFe/(La-PCM) NPs in 4T1 cells was tested by using the O_2 probe RDPP, whose fluorescence can be immediately quenched by O_2. As displayed in Fig. 5B and Fig. 5D, a decreased fluorescence signal was observed, which was mainly caused by the O_2 evolution via the catalytic reaction, as compared to the control. The findings suggest that CV@PtFe/(La-PCM) NPs also have high catalytic activity within cells. On the other hand, the NIR laser irradiation enhanced engenders ample highly cytotoxic •OH and the La contributed to the enhanced.

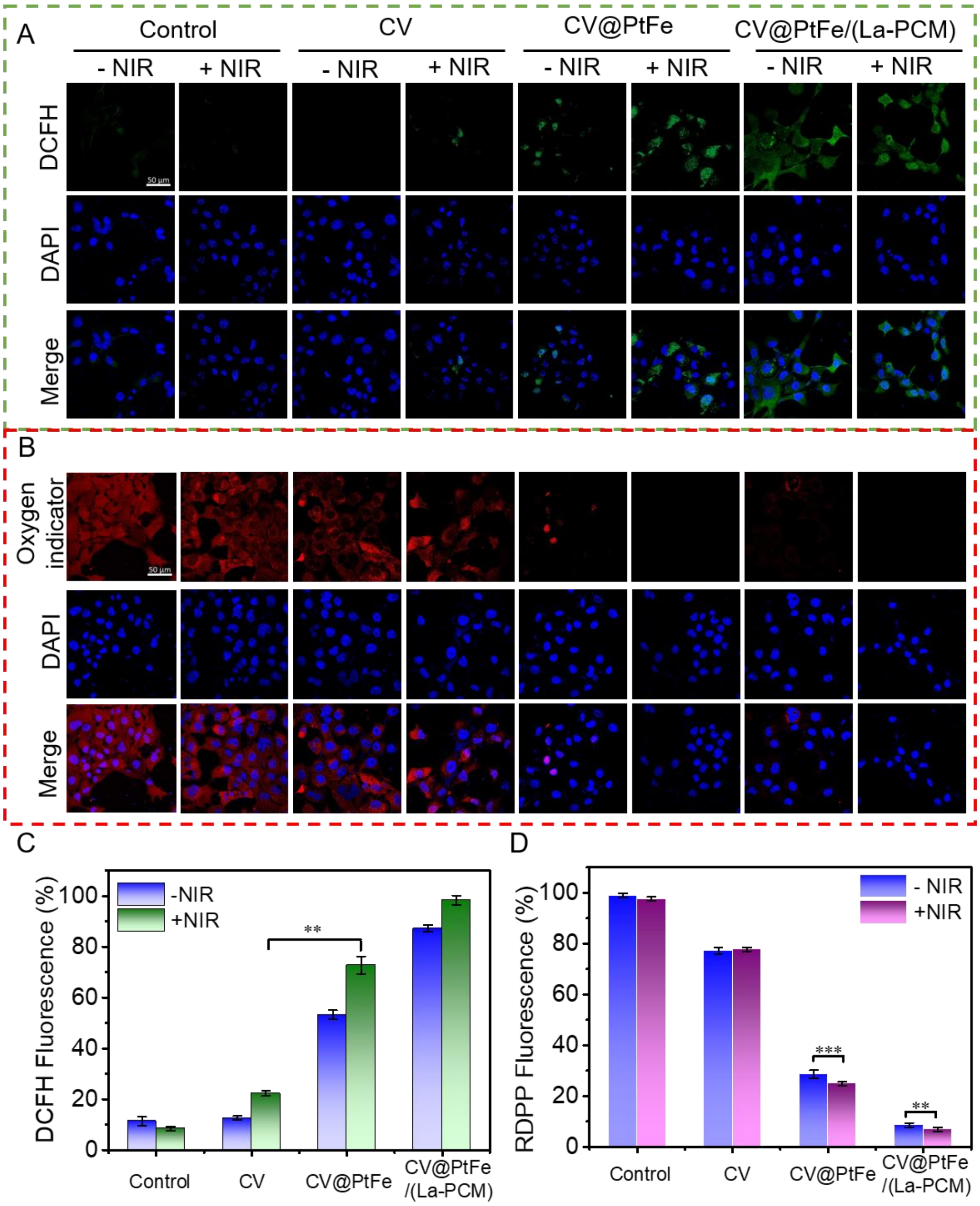

Fig. 5. (A) Fluorescence images of 4T1 cells stained by DCFH-DA to indicate nanoparticle-induced ROS generation and (B) CLSM images of 4T1 cells stained by RDPP after treatment with different groups. (C and D) Statistical analysis of relative

DCFH and RDPP fluorescence (%).

3.5 In vitro *anti-tumor properties*

The schematic diagram in Fig. 6A illustrates the proposed working mechanism of CV@PtFe/(La-PCM) NPs, which is mainly driven by the NIR-mediated mild temperature photothermal and synergistic catalytic conversion of H_2O_2 to highly toxic •OH. This is referred to as oxidative stress, which then goes on to destroy DNA molecules through oxidation, inducing cellular apoptosis.

In a subsequent step, the antitumor activity of the nanocatalyst was investigated by CCK-8 assay; 4T1 cell viability cultured with CV@PtFe/(La-PCM) NPs with or without 808 nm NIR laser irradiation. As shown in Fig. 6B, according to the CCK-8 data, the 4T1 cells treated with CV@PtFe/(La-PCM) NPs under NIR laser irradiation showed the highest cell death, with concentration dependent behavior. The cell viability of similar concentrations without NIR irradiation had lower toxicity for 4T1 cells. This could be attributed to the NIR laser irradiation heating the surroundings, which accelerates the release of La and improves the synergistic therapeutic effect. To intuitively display the antitumor efficiency of CV@PtFe/(La-PCM) NPs with or without 808 nm laser irradiation. Live–dead cell staining was performed by Calcein-AM/PI double staining and was observed by CLSM. The red fluorescence signal represents dead cells and the green fluorescence represents live cells. As illustrated in Fig. 6C, the cells treated with CV@PtFe/(La-PCM) NPs without NIR laser irradiation showed few dead cells. Notably, the cells were destroyed after treatment with

CV@PtFe/(La-PCM) NPs under NIR laser irradiation, compared to the negative control group, which was consistent with the CCK-8 assay results. These results demonstrate that the synergy between the PtFe NP catalyzing center and La enhances intracellular H_2O_2 formation under NIR laser irradiation and is essential for H_2O_2-enhanced combination therapy of the nanocatalyst. Moreover, the antitumor efficiency of the nanocatalyst was further examined via JC-1 staining (Fig. 6D). The change in membrane potential could thus be evaluated by analysis of the green (depolarized mitochondria)/red (normal mitochondria) fluorescence intensity ratio. As expected, the group treated with CV@PtFe/(La-PCM) NPs with NIR laser irradiation exhibited the highest fluorescence ratio of green monomer to red aggregate, indicating that abundant mitochondria were dysfunctional. This further confirmed the excellent anticancer efficacy of the combined simultaneous approach being far superior to any individual modality.

This was also accompanied with severe DNA damage, as the quantitative western blot analysis on the expression levels of the DNA damage-associated protein γ-H2AX (H2A histone family member X) in the CV@PtFe/(La-PCM) NPs with laser irradiation group was 3.4-fold higher than the control (Fig. S13).

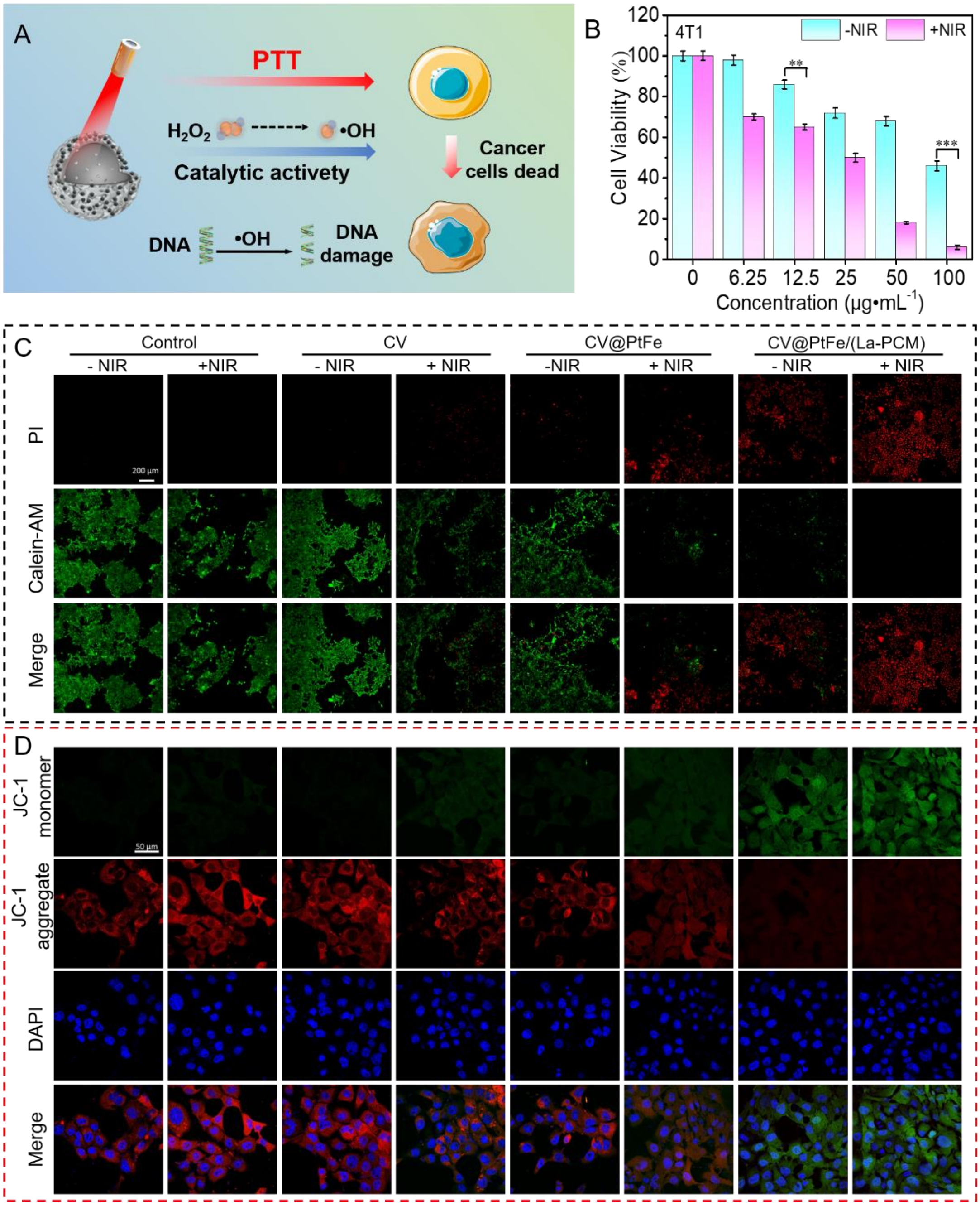

Fig. 6. (A) Schematic diagram of the anticancer mechanism of CV@PtFe/(La-PCM) NPs. (B) Relative viabilities of 4T1 cells after being incubated with CV@PtFe/(La-PCM) NPs at varying solution concentrations with or without NIR laser irradiation. (C) Fluorescence images of 4T1 cells co-stained with Calcein AM/PI after being treated with different preparations. Live and dead cells displayed green and red signals, respectively. (D) Detection of MMP stained with JC-1 of CV NPs, CV@PtFe NPs and

CV@PtFe/(La-PCM) NPs by CLSM.

3.6 The molecular mechanism CV@PtFe/(La-PCM) NP-mediated photothermally regulated cell death

Based on the results of *in vitro* assays and literature reports, the detailed molecular mechanism of CV@PtFe/(La-PCM) NP-mediated photothermally regulated cell death can be summarized as displayed in Fig. 7A. To investigate if HSP70 could stabilize and upregulate NAD(P)H: quinone oxidoreductase protein (NQO1) in tumor cells and induce intracellular H_2O_2 generation by La, a western blot analysis was performed, further exploring the molecular mechanism of CV@PtFe/(La-PCM) NP-mediated photothermally regulated protein expression in the tumor cell. Key biomarker changes in HSP70 and NQO1 expression showed that the expression levels of HSP70 and NQO1 were positively linked to the total NIR dose, revealing the cellular impact of the nanocatalyst-mediated photothermal effect (Fig. 7B and Fig. 7C). Immunofluorescence imaging results consistently revealed that without NIR laser irradiation, all sample groups had insignificant HSP70 and NQO1 expression, which was dramatically increased under NIR laser irradiation (Fig. 7D). Together, these data demonstrate that CV@PtFe/(La-PCM) NP-mediated, NIR-actuated photothermal effect increase NQO1 expression via HSP70/NQO1 axis.

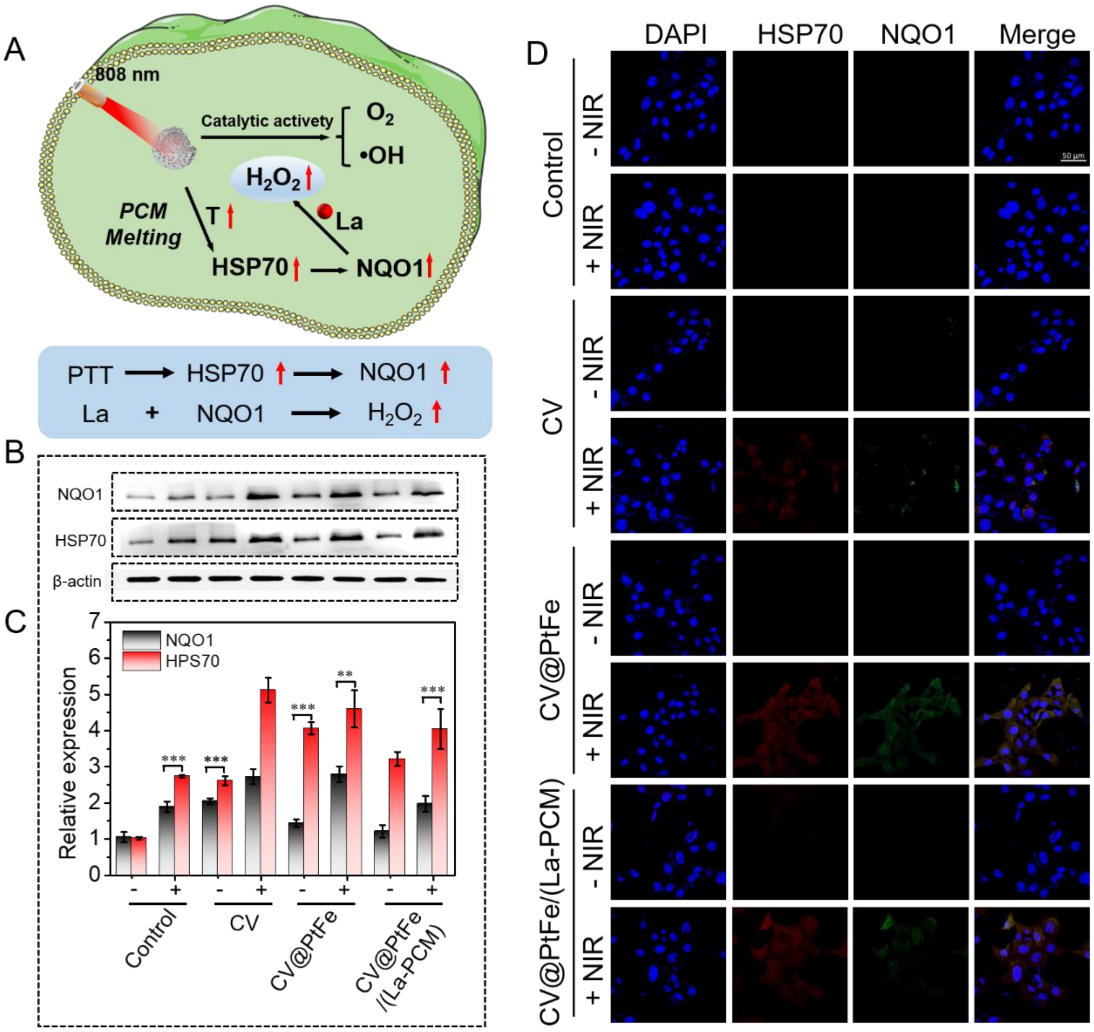

Fig. 7. (A) The molecular mechanism of CV@PtFe/(La-PCM) NP-mediated photothermally regulated cell death. (B) Western blot analysis on the expression of key therapeutic biomarkers of HSP70 and NQO1 of 4T1 cells after incubation with CV NPs, CV@PtFe NPs and CV@PtFe/(La-PCM) NPs for 24 h with or without NIR laser irradiation. (C) Quantitative western blot analysis on the expression levels of key biomarkers, HSP70 and NQO1, after different treatments. (D) HSP70 and NQO1 immunofluorescence on the 4T1 cells after incubation with different preparation for 24 h (HSP70: red; NQO1: green; blue: cell nucleus).

3.7 In vivo *tumor accumulation capability and photothermal ability of CV@PtFe/(La-PCM) NPs*

Before evaluating the anticancer efficacy, the potential photothermal efficacy of CV@PtFe/(La-PCM) NPs with NIR laser irradiation *in vivo* was checked. A NIR thermal imaging camera was chosen to probe the photothermal behavior in 4T1 tumor-bearing mice. As shown in Fig. 8A and Fig. 8C, under NIR laser irradiation, the tumor temperature in mice receiving CV@PtFe/(La-PCM) NP groups was much higher and increased rapidly by 8.2 °C within 5 min, which was a suitable temperature to activate cellular heat shock response and upregulate the downstream NQO1 via HSP70/NQO1 axis to facilitate bio-reduction of the concurrently released La and enhance intracellular H_2O_2 formation, while the local temperature of the saline-treated group only increased by approximately 1.2 °C after the same NIR laser irradiation exposure. These findings suggest that the CV@PtFe/(La-PCM) NP system is an effective agent of PTT for tumor ablation *in vivo*. Then, to evaluate the tumor accumulation capability of Cy7-labelled CV@PtFe/(La-PCM) NPs, Cy7-CV@PtFe/(La-PCM) NPs was administered intravenously into the 4T1 tumor-bearing mice for *in vivo* fluorescence imaging. As displayed in Fig. 8B and Fig. 8D, and taking advantage of the EPR effect, the significantly brighter fluorescence at 8 h and the gradual enrichment of fluorescence at the tumor site was also observed for the mice treated with Cy7-CV@PtFe/(La-PCM) NPs, demonstrating that Cy7-CV@PtFe/(La-PCM) NPs could accumulate in tumor obviously after injection. Next, various mice organs (heart, liver, spleen, lung, and kidney) and tumors were obtained from the mice 24 h after injection, to further evaluate their ability to accumulate in the tumor site. As shown in the *in vivo* fluorescence images, tumor tissues gave stronger fluorescence signals than other organs. It suggests the high specific accumulation of the nanocatalyst through passive targeting (EPR effect) and the advantages in enhancing anticancer efficacy while reducing the side effects of free drug. The liver also gave a relatively strong fluorescent signal because the liver was the most important detoxifying organ, which is responsible for metabolizing and clearance of CV@PtFe/(La-PCM) NPs *in vivo*.

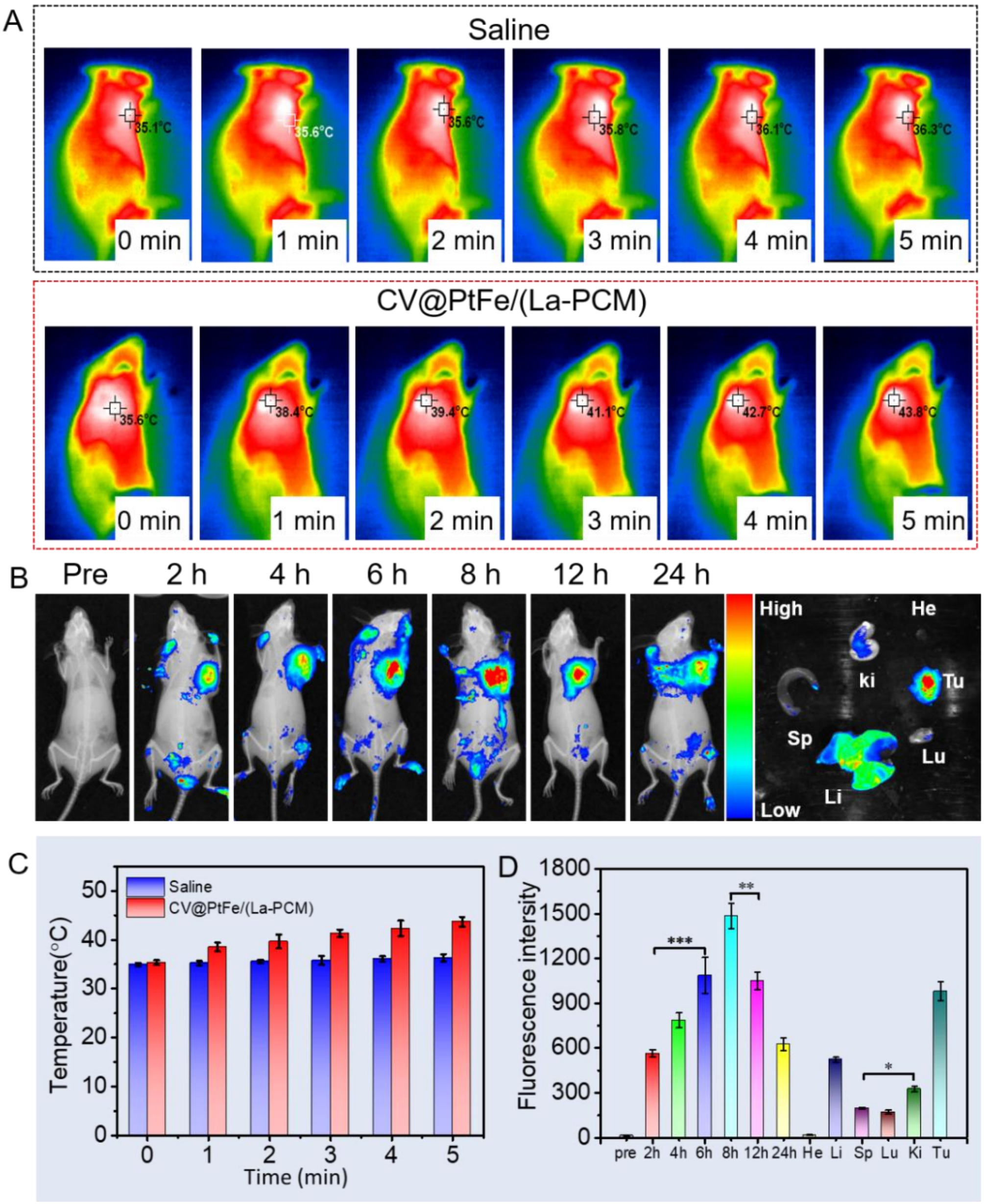

Fig. 8. (A) NIR thermal graphs of 4T1 tumor-bearing mice after intravenous injection with saline, CV@PtFe/(La-PCM) NPs for 12 h and then treated with NIR (808 nm, 1 W·cm^{-2}) laser irradiation. (B) Real-time fluorescence imaging of 4T1 tumor-bearing mice before and after intravenous injection of Cy7-labeled CV@PtFe/(La-PCM) NPs. (C) *In vivo* temperature recorded in real time. (D) Semiquantitative analysis of fluorescence intensity of the major organs and tumor tissues collected at 24 h after injection of Cy7-labeled CV@PtFe/(La-PCM) NPs.

3.8 In Vivo *therapeutic effects evaluation*

Based on the excellent synergistic antitumor efficacy of CV@PtFe/(La-PCM) NPs with NIR laser irradiation on the cellular level and active targeted accumulation at the tumor sites, the *in vivo* combined therapeutic efficacy was further studied using 4T1 tumor-bearing mice and the therapeutic process is shown in Fig. 9A. The mice were randomly divided into 5 groups and treated with saline, CV NPs, CV@PtFe NPs and CV@PtFe/(La-PCM) NPs with or without exposure to NIR laser irradiation for 5 min after 8 h injection, respectively. The tumor sizes and weights of mice were measured every two days after treatment. As shown in the photographic images of tumors and mice, the tumor growth was almost completely suppressed in the group treated with CV@PtFe/(La-PCM) NPs and exposed to laser irradiation (Fig. 9B and Fig. 9C). In contrast, the CV NPs, CV@PtFe NPs with NIR groups did not show a significant antitumor effect. Furthermore, the mice injected with CV NPs and CV@PtFe NPs, without laser irradiation exhibited tumor growths similar to those mice injected with only saline. Promisingly, the tumor volume and weight in the combination therapy group was the most significantly reduced, confirming that the synergistic approach exhibited excellent therapeutic effect (Fig. 9D and Fig. 9F). Our findings also revealed that hyperthermia at a low temperature of 43 °C would be sufficient for effective tumor ablation.

Histological hematoxylin and eosin (H&E) analysis was used to evaluate the potential destruction of tumor tissues. As shown in Fig. 9G, compared to the control groups, serious cell damage, cell interspace increase and a larger number of apoptotic cells with extensive nuclear shrinkage were observed in the tumors of the mice treated with CV@PtFe/(La-PCM) NPs exposed to NIR laser irradiation. The results were further confirmed by the high proportion of positive cells stained with TUNEL and Ki-67. In the meantime, benefiting from the low systemic toxicity, as shown in Fig. 9E, only minor fluctuations in the body weight of the mice was observed in each treatment group. The H&E staining of the main organs from our combination therapy-treated mice also showed no obvious change in each group after treatment (Fig. S14). The above results confirmed that combination therapy (*i.e.* CV@PtFe/(La-PCM) NPs with NIR laser irradiation) has no notable toxicities on the whole body and exhibits excellent tumor inhibition efficacy.

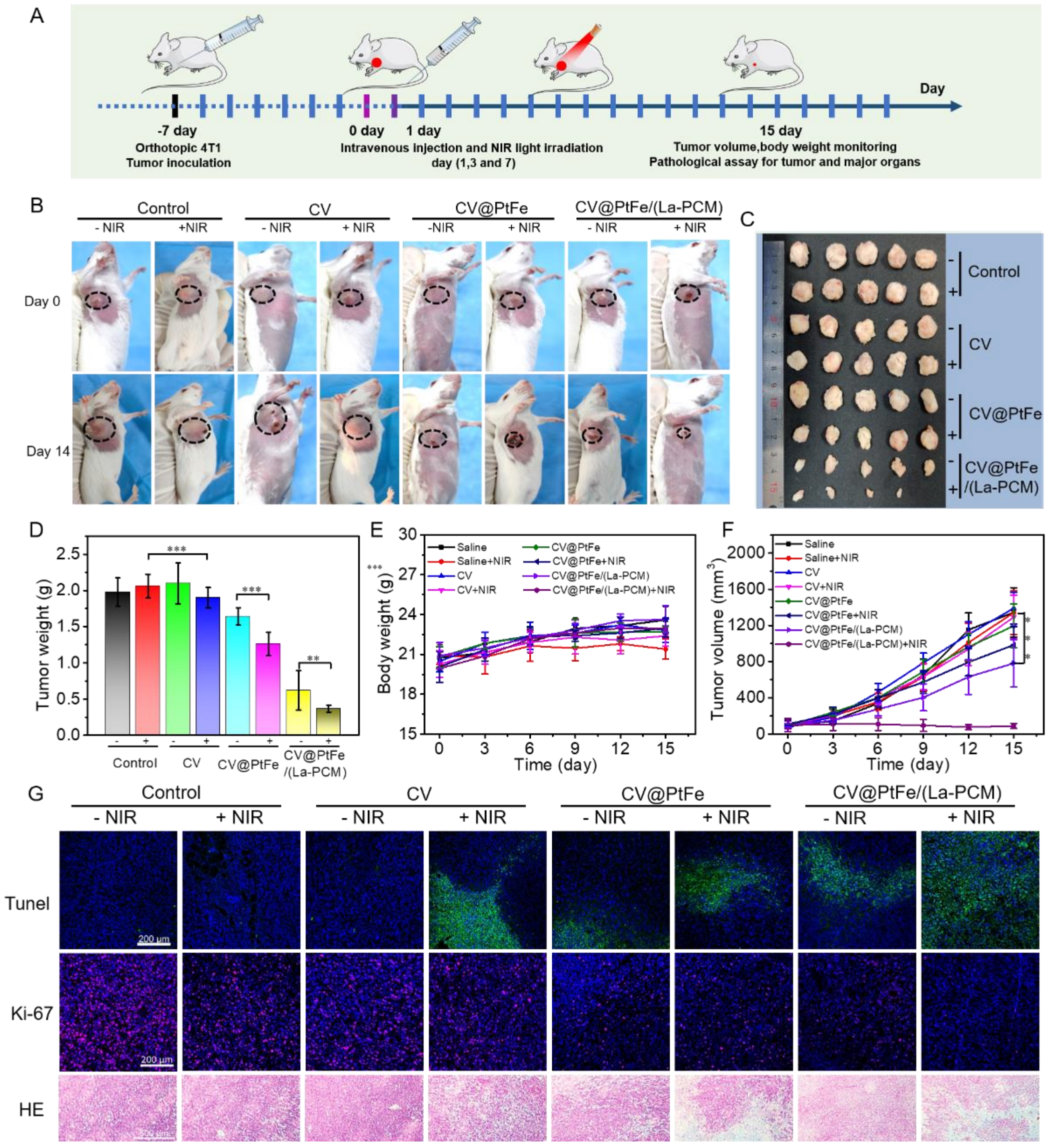

Fig. 9. (A) Schematic illustration of the therapy scheme involving the comparison of injections with saline, CV NPs, CV@PtFe NPs and CV@PtFe/(La-PCM) NPs with or without NIR laser irradiation, respectively, and records of tumor sizes, images and body mass. (B) Representative digital photographic images of 4T1 tumor-bearing mice after different treatments at 0 and 15 days. (C) Digital pictures of a tumor from the 4T1 mice after 15 days of different treatment. (D) The average tumor mass after 15 days of treatment. (E) and (F) body mass and relative tumor volume during the treatment. (G) Histological analysis of tumor biopsies after different treatment through

immunostaining with TUNEL, H&E and Ki-67.

4. Conclusion

In summary, a near-infrared light-responsive nanocatalyst as an intelligent drug release system was developed for synergistic cooperation with mild-temperature photothermal and catalytic therapy for enhanced tumor treatment. The nanoplatform was successfully synthesized by direct synthesis of PtFe nanoparticles (PtFe NPs) loaded onto carbon vesicle (CV) supports. The highly porous CV@PtFe NPs were loaded with a mixture of β-lapachone (La) and phase change material (PCM). The CV@PtFe/(La-PCM) NPs can be uniformly dispersed in the physiological environment with high long-term stability. Crucially, the PtFe NPs were able to oxidize the intracellular H_2O_2 to produce highly toxic •OH and O_2, which was used for cancer nanocatalytic therapy. The photothermal effect of CV@PtFe/(La-PCM) NPs allows the PCM to be melted PCM and concomitantly release La under NIR laser irradiation, which in turn elevated intracellular H_2O_2 formation to promote PtFe NP catalytic activity. Attributed to the EPR effect, the tumor accumulation was significantly improved, favorable in enhancing the antitumor performance and reducing side effects. Both *in vitro* and *in vivo* assays confirmed that the remarkable synergistic therapeutic effect of CV@PtFe/(La-PCM) NPs enabled mild-photothermal nanocatalytic therapy to be amplified, where a vast amount of highly oxidizing •OH and local hyperthermia could suppress tumor growth. Thus, this work has provided a biosynthetic strategy for self-enhancing nanocatalytic therapy combined with mild-photothermal behavior, which opens a window for future nanocatalyst design and tumor treatment.

CRediT authorship contribution statement

Mengmeng Xu: Conceptualization, Methodology, Validation, Formal analysis, Investigation, Data curation, Writing - original draft, Writing, review & editing. **Yuan Liu**: Validation, Formal analysis. **Xiaoqi Xie**: Validation, Formal analysis. **Paul D. Topham**: validation, writing, review and editing. **Yuandong Zeng**: Formal analysis. **Jilai Zhan**: Investigation. **LinGe Wang**: Conceptualization, Resources, Writing - review & editing, Supervision, Funding acquisition. **Qianqian Yu**: Conceptualization, Resources, Supervision, Funding acquisition.

Declaration of competing interest

The authors declare that they have no known competing financial interests or personal relationships that could have appeared to influence the work reported in this paper.

Acknowledgments

The authors thank the financial support from National Natural Science Foundation of China (No. U22A20316 and 21807046), Guangdong Province Basic and Applied Basic Research Fund Project (No. 2023? And 2021A1515111174), Guangdong Project (No. 2016ZT06C322), and Overseas Expertise Introduction Center for Discipline Innovation ("111 Center").

References

[1] W. Chen, J. Ouyang, H. Liu, M. Chen, K. Zeng, J. Sheng, Z. Liu, Y. Han, L. Wang, J. Li, L. Deng, Y.N. Liu, S. Guo, Black Phosphorus Nanosheet-Based Drug Delivery System for Synergistic Photodynamic/Photothermal/Chemotherapy of Cancer, Adv. Mater. 29(5) (2017) 1603276.

[2] R. Lv, P. Yang, F. He, S. Gai, G. Yang, Y. Dai, Z. Hou, J. Lin, An imaging-guided platform for synergistic photodynamic/photothermal/chemo-therapy with pH/temperature-responsive drug release, Biomaterials 63 (2015) 115-127.

[3] M.-R. Chiang, Y.-L. Su, C.-Y. Chang, C.-W. Chang, S.-H. Hu, Lung metastasis-targeted donut-shaped nanostructures shuttled by the margination effect for the PolyDox generation-mediated penetrative delivery into deep tumors, Mater. Horizons 7(4) (2020) 1051-1061.

[4] Y. Liu, P. Bhattarai, Z. Dai, X. Chen, Photothermal therapy and photoacoustic imaging via nanotheranostics in fighting cancer, Chem. Soc. Rev. 48(7) (2019) 2053-2108.

[5] W. Wu, L. Yu, Q. Jiang, M. Huo, H. Lin, L. Wang, Y. Chen, J. Shi, Enhanced Tumor-Specific Disulfiram Chemotherapy by In Situ Cu^{2+} Chelation-Initiated Nontoxicity-to-Toxicity Transition, J. Am. Chem. Soc. 141(29) (2019) 11531-11539.

[6] H. Lin, Y. Chen, J. Shi, Nanoparticle-triggered in situ catalytic chemical reactions for tumour-specific therapy, Chem. Soc. Rev. 47(6) (2018) 1938-1958.

[7] C. Matera, A.M.J. Gomila, N. Camarero, M. Libergoli, C. Soler, P. Gorostiza, Photoswitchable Antimetabolite for Targeted Photoactivated Chemotherapy, J. Am. Chem. Soc. 140(46) (2018) 15764-15773.

[8] C. Wang, X. Jia, W. Zhen, M. Zhang, X. Jiang, Small-Sized MOF-Constructed Multifunctional Diagnosis and Therapy Platform for Tumor, ACS Biomater. Sci. Eng. 5(9) (2019) 4435-4441.

[9] P. Agostinis, K. Berg, K.A. Cengel, T.H. Foster, A.W. Girotti, S.O. Gollnick, S.M. Hahn, M.R. Hamblin, A. Juzeniene, D. Kessel, M. Korbelik, J. Moan, P. Mroz, D. Nowis, J. Piette, B.C. Wilson, J. Golab, Photodynamic therapy of cancer: an update,

CA Cancer J. Clin. 61(4) (2011) 250-281.

[10] Y. Liu, H. Gou, X. Huang, G. Zhang, K. Xi, X. Jia, Rational synthesis of highly efficient ultra-narrow red-emitting carbon quantum dots for NIR-II two-photon bioimaging, Nanoscale 12(3) (2020) 1589-1601.

[11] Y. Li, S. Zeng, J. Hao, Non-Invasive Optical Guided Tumor Metastasis/Vessel Imaging by Using Lanthanide Nanoprobe with Enhanced Down-Shifting Emission beyond 1500 nm, ACS Nano 13(1) (2019) 248-259.

[12] R. Hu, Y. Fang, M. Huo, H. Yao, C. Wang, Y. Chen, R. Wu, Ultrasmall Cu_2-xS nanodots as photothermal-enhanced Fenton nanocatalysts for synergistic tumor therapy at NIR-II biowindow, Biomaterials 206 (2019) 101-114.

[13] X. Huang, N. Mu, Y. Ding, H.W. Lam, L. Yue, C. Gao, T. Chen, Z. Yuan, R. Wang, Targeted delivery and enhanced uptake of chemo-photodynamic nanomedicine for melanoma treatment, Acta Biomater. 147 (2022) 356-365.

[14] C. Jiang, T. He, Q. Tang, J. He, Q. Ren, D.-Y. Zhang, B. Gurram, N.T. Blum, Y. Chen, P. Huang, J. Lin, Nanozyme catalyzed cascade reaction for enhanced chemodynamic therapy of low-H_2O_2 tumor, Appl. Mater. Today 26 (2022) 101357-101364.

[15] Z. Xiao, W. Zuo, L. Chen, L. Wu, N. Liu, J. Liu, Q. Jin, Y. Zhao, X. Zhu, H_2O_2 Self-Supplying and GSH-Depleting Nanoplatform for Chemodynamic Therapy Synergetic Photothermal/Chemotherapy, ACS Appl. Mater. Interfaces 13(37) (2021) 43925-43936.

[16] B. Liu, Y. Bian, S. Liang, M. Yuan, S. Dong, F. He, S. Gai, P. Yang, Z. Cheng, J. Lin, One-Step Integration of Tumor Microenvironment-Responsive Calcium and Copper Peroxides Nanocomposite for Enhanced Chemodynamic/Ion-Interference Therapy, ACS Nano 16(1) (2021) 617-630.

[17] J. Zhai, J. Gao, J. Zhang, D. Liu, S. Gao, Y. Yan, K. Zhang, K. Cai, F. Yu, M. Lin, J. Li, Concave Octahedral PtCu Nanoframes Mediated Synergetic Photothermal and Chemodynamic Tumor Therapy, Chem. Eng. J. 442 (2022) 136172.

[18] J. Yang, H. Yao, Y. Guo, B. Yang, J. Shi, Enhancing Tumor Catalytic Therapy by

Co-Catalysis, Angew. Chem. Int.Ed. 61(17) (2022) e202200480.

[19] X. Wang, C. Li, H. Jin, X. Wang, C. Ding, D. Cao, L. Zhao, G. Deng, J. Lu, Z. Wan, X. Liu, Mutual promotion of oxidative stress amplification and calcium overload by degradable spatially selective self-cascade catalyst for synergistic tumor therapy, Chem. Eng. J. 432 (2022) 134438.

[20] Y. Zhao, W. Zhang, Y. Lin, D. Du, The vital function of Fe_3O_4@Au nanocomposites for hydrolase biosensor design and its application in detection of methyl parathion, Nanoscale 5(3) (2013) 1121-6.

[21] S. Fang, C. Wang, J. Xiang, L. Cheng, X. Song, L. Xu, R. Peng, Z. Liu, Aptamer-conjugated upconversion nanoprobes assisted by magnetic separation for effective isolation and sensitive detection of circulating tumor cells, Nano Res. 7(9) (2014) 1327-1336.

[22] M. Wang, M. Chang, Q. Chen, D. Wang, C. Li, Z. Hou, J. Lin, D. Jin, B. Xing, Au_2Pt-PEG-Ce6 nanoformulation with dual nanozyme activities for synergistic chemodynamic therapy / phototherapy, Biomaterials 252 (2020) 120093.

[23] X.C. Hu, E. Agostinelli, C. Ni, G.C. Hadjipanayis, A. Capobianchi, A low temperature and solvent-free direct chemical synthesis of L10 FePt nanoparticles with size tailoring, Green Chem. 16(4) (2014) 2292-2297.

[24] X. Ji, Y. Kang, J. Ouyang, Y. Chen, D. Artzi, X. Zeng, Y. Xiao, C. Feng, B. Qi, N.Y. Kim, P.E. Saw, N. Kong, O.C. Farokhzad, W. Tao, Synthesis of Ultrathin Biotite Nanosheets as an Intelligent Theranostic Platform for Combination Cancer Therapy, Adv. Sci. 6(19) (2019) 1901211.

[25] H. Wang, Y. Chao, J. Liu, W. Zhu, G. Wang, L. Xu, Z. Liu, Photosensitizer-crosslinked in-situ polymerization on catalase for tumor hypoxia modulation & enhanced photodynamic therapy, Biomaterials 181 (2018) 310-317.

[26] Z. Tang, H. Zhang, Y. Liu, D. Ni, H. Zhang, J. Zhang, Z. Yao, M. He, J. Shi, W. Bu, Antiferromagnetic Pyrite as the Tumor Microenvironment-Mediated Nanoplatform for Self-Enhanced Tumor Imaging and Therapy, Adv. Mater. 29(47) (2017) 1701683.

[27] W. Li, X. Zhou, S. Liu, J. Zhou, H. Ding, S. Gai, R. Li, L. Zhong, H. Jiang, P. Yang,

Biodegradable Nanocatalyst with Self-Supplying Fenton-like Ions and H_2O_2 for Catalytic Cascade-Amplified Tumor Therapy, ACS Appl. Mater. Interfaces 13(43) (2021) 50760-50773.

[28] Y. He, S. Guo, Y. Zhang, Y. Liu, H. Ju, NIR-II reinforced intracellular cyclic reaction to enhance chemodynamic therapy with abundant H_2O_2 supply, Biomaterials 275 (2021) 120962.

[29] X. Wang, X. Zhong, Z. Liu, L. Cheng, Recent progress of chemodynamic therapy-induced combination cancer therapy, Nano Today 35 (2020) 100946.

[30] Z. Gu, S. Zhu, L. Yan, F. Zhao, Y. Zhao, Graphene-Based Smart Platforms for Combined Cancer Therapy, Adv. Mater. 31(9) (2019) e1800662.

[31] M. Xu, Y. Liu, W. Luo, F. Tan, D. Dong, W. Li, L. Wang, Q. Yu, A multifunctional nanocatalytic system based on Chemodynamic-Starvation therapies with enhanced efficacy of cancer treatment, J. Colloid Interface Sci. 630 (2023) 804-816.

[32] M. Xu, H. Zhou, Y. Liu, J. Sun, W. Xie, P. Zhao, J. Liu, Ultrasound-Excited Protoporphyrin IX-Modified Multifunctional Nanoparticles as a Strong Inhibitor of Tau Phosphorylation and beta-Amyloid Aggregation, ACS Appl. Mater. Interfaces 10(39) (2018) 32965-32980.

[33] X. Wang, X. Zhong, Z. Zha, G. He, Z. Miao, H. Lei, Q. Luo, R. Zhang, Z. Liu, L. Cheng, Biodegradable CoS_2 nanoclusters for photothermal-enhanced chemodynamic therapy, Appl. Mater. Today 18 (2020) 100464.

[34] Y. Liu, W. Zhen, Y. Wang, J. Liu, L. Jin, T. Zhang, S. Zhang, Y. Zhao, S. Song, C. Li, J. Zhu, Y. Yang, H. Zhang, One-Dimensional Fe_2P Acts as a Fenton Agent in Response to NIR II Light and Ultrasound for Deep Tumor Synergetic Theranostics, Angew. Chem. Int. Ed. 58(8) (2019) 2407-2412.

[35] G. Chen, Y. Cao, Y. Tang, X. Yang, Y. Liu, D. Huang, Y. Zhang, C. Li, Q. Wang, Advanced Near-Infrared Light for Monitoring and Modulating the Spatiotemporal Dynamics of Cell Functions in Living Systems, Adv. Sci. 7(8) (2020) 1903783.

[36] Y. Liu, J. Wu, Y. Jin, W. Zhen, Y. Wang, J. Liu, L. Jin, S. Zhang, Y. Zhao, S. Song, Y. Yang, H. Zhang, Copper(I) Phosphide Nanocrystals for In Situ Self-Generation

Magnetic Resonance Imaging-Guided PhotothermalEnhanced Chemodynamic Synergetic Therapy Resisting Deep-Seated Tumor, Adv. Funct. Mater. 29(50) (2019) 1904678.

[37] L. Chen, X. Sun, K. Cheng, P.D. Topham, M. Xu, Y. Jia, D. Dong, S. Wang, Y. Liu, L. Wang, Q. Yu, Temperature-Regulating Phase Change Fiber Scaffold Toward Mild Photothermal–Chemotherapy, Adv.Fiber Mater. (4) (2022) 1669–1684.

[38] L. Chen, D. Zhang, K. Cheng, W. Li, Q. Yu, L. Wang, Photothermal-responsive fiber dressing with enhanced antibacterial activity and cell manipulation towards promoting wound-healing, J. Colloid Interface Sci. 623 (2022) 21-33.

[39] W. Zuo, Z. Fan, L. Chen, J. Liu, Z. Wan, Z. Xiao, W. Chen, L. Wu, D. Chen, X. Zhu, Copper-based theranostic nanocatalysts for synergetic photothermal-chemodynamic therapy, Acta Biomater. 147 (2022) 258-269.

[40] X. Cui, G. Lu, F. Fang, Y. Xiong, S. Tian, Y. Wan, Y. Xiao, D. Shen, H. Wang, J. Zhang, C.S. Lee, Iron Self-Boosting Polymer Nanoenzyme for Low-Temperature Photothermal-Enhanced Ferrotherapy, ACS Appl. Mater. Interfaces 13(26) (2021) 30274-30283.

[41] Y. Yang, W. Zhu, Z. Dong, Y. Chao, L. Xu, M. Chen, Z. Liu, 1D Coordination Polymer Nanofibers for Low-Temperature Photothermal Therapy, Adv. Mater. 29(40) (2017) 1703588.

[42] Y. Jiang, X. Zhao, J. Huang, J. Li, P.K. Upputuri, H. Sun, X. Han, M. Pramanik, Y. Miao, H. Duan, K. Pu, R. Zhang, Transformable hybrid semiconducting polymer nanozyme for second near-infrared photothermal ferrotherapy, Nat. Commun. 11(1) (2020) 1857.

[43] C. Xue, M. Li, C. Liu, Y. Li, Y. Fei, Y. Hu, K. Cai, Y. Zhao, Z. Luo, NIR-Actuated Remote Activation of Ferroptosis in Target Tumor Cells through a Photothermally Responsive Iron-Chelated Biopolymer Nanoplatform, Angew. Chem. Int.Ed. 60 (2021) 6-12.

[44] X. Li, Z. Liu, A. Zhang, C. Han, A. Shen, L. Jiang, D.A. Boothman, J. Qiao, Y. Wang, X. Huang, Y.X. Fu, NQO1 targeting prodrug triggers innate sensing to overcome

checkpoint blockade resistance, Nat. Commun. 10(1) (2019) 3251.

[45] E. Blanco, E.A. Bey, C. Khemtong, S.G. Yang, J. Setti-Guthi, H. Chen, C.W. Kessinger, K.A. Carnevale, W.G. Bornmann, D.A. Boothman, J. Gao, Beta-lapachone micellar nanotherapeutics for non-small cell lung cancer therapy, Cancer Res. 70(10) (2010) 3896-904.

[46] M. Ye, Y. Han, J. Tang, Y. Piao, X. Liu, Z. Zhou, J. Gao, J. Rao, Y. Shen, A Tumor-Specific Cascade Amplification Drug Release Nanoparticle for Overcoming Multidrug Resistance in Cancers, Adv. Mater. 29(38) (2017) 1702342.

[47] X. Ma, X. Huang, Z. Moore, G. Huang, J.A. Kilgore, Y. Wang, S. Hammer, N.S. Williams, D.A. Boothman, J. Gao, Esterase-activatable beta-lapachone prodrug micelles for NQO1-targeted lung cancer therapy, J. Control. Release 200 (2015) 201-11.

[48] Z. Jiang, B. Yuan, Y. Wang, Z. Wei, S. Sun, O.U. Akakuru, Y. Li, J. Li, A. Wu, Near-infrared heptamethine cyanine dye-based nanoscale coordination polymers with intrinsic nucleus-targeting for low temperature photothermal therapy, Nano Today 34 (2020) 100910.

[49] M. Chang, Z. Hou, M. Wang, C. Yang, R. Wang, F. Li, D. Liu, T. Peng, C. Li, J. Lin, Single-Atom Pd Nanozyme for Ferroptosis-Boosted Mild-Temperature Photothermal Therapy, Angew. Chem. Int. Ed. 60(23) (2021) 12971-12979.

[50] Q. Chen, C. Zhu, D. Huo, J. Xue, H. Cheng, B. Guan, Y. Xia, Continuous processing of phase-change materials into uniform nanoparticles for near-infrared-triggered drug release, Nanoscale 10(47) (2018) 22312-22318.

[51] J. Qiu, D. Huo, Y. Xia, Phase-Change Materials for Controlled Release and Related Applications, Adv. Mater. 32(25) (2020) e2000660.

[52] F. Wang, Z. Yuan, P. McMullen, R. Li, J. Zheng, Y. Xu, M. Xu, Q. He, B. Li, H. Chen, Near-Infrared-Light-Responsive Lipid Nanoparticles as an Intelligent Drug Release System for Cancer Therapy, Chem. Mater. 31(11) (2019) 3948-3956.

[53] J. Qiu, D. Huo, J. Xue, G. Zhu, H. Liu, Y. Xia, Encapsulation of a Phase-Change Material in Nanocapsules with a Well-Defined Hole in the Wall for the Controlled

Release of Drugs, Angew. Chem. Int.Ed. 58(31) (2019) 10606-10611.

[54] J. Guo, D. Li, Z. Qian, H. Luo, M. Yang, Q. Wang, J. Xu, N. Zhao, Carbon Vesicles: A Symmetry-Breaking Strategy for Wide-Band and Solvent-Processable Ultrablack Coating Materials, Adv. Funct. Mater. 30(17) (2020) 1909877.

[55] T.Y. Yoo, J.M. Yoo, A.K. Sinha, M.S. Bootharaju, E. Jung, H.S. Lee, B.H. Lee, J. Kim, W.H. Antink, Y.M. Kim, J. Lee, E. Lee, D.W. Lee, S.P. Cho, S.J. Yoo, Y.E. Sung, T. Hyeon, Direct Synthesis of Intermetallic Platinum-Alloy Nanoparticles Highly Loaded on Carbon Supports for Efficient Electrocatalysis, J. Am. Chem. Soc 142(33) (2020) 14190-14200.

[56] H. Yang, B. Xu, S. Li, Q. Wu, M. Lu, A. Han, H. Liu, A Photoresponsive Nanozyme for Synergistic Catalytic Therapy and Dual Phototherapy, Small 17(10) (2021) e2007090.

[57] Y. Li, G. Bai, S. Zeng, J. Hao, Theranostic Carbon Dots with Innovative NIR-II Emission for in Vivo Renal-Excreted Optical Imaging and Photothermal Therapy, ACS Appl. Mater. Interfaces 11(5) (2019) 4737-4744.